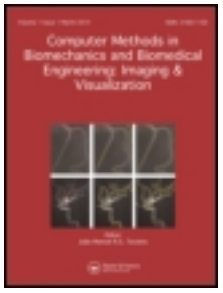

Computer Methods in Biomechanics and Biomedical Engineering: Imaging & Visualization
Publication details, including instructions for authors and subscription information:
http://www.tandfonline.com/loi/tciv20

A 3D low-cost solution for the aesthetic evaluation of breast cancer conservative treatment

Hélder P. Oliveira[a], Jaime S. Cardoso[a], André T. Magalhães[b] & Maria J. Cardoso[c]
[a] INESC TEC and Faculdade de Engenharia, Universidade do Porto, Porto, Portugal
[b] Faculdade de Medicina, Universidade do Porto, Porto, Portugal
[c] Breast Unit, Champalimaud Cancer Center, Champalimaud Foundation, Lisboa, Portugal
Published online: 13 Dec 2013.

To cite this article: Hélder P. Oliveira, Jaime S. Cardoso, André T. Magalhães & Maria J. Cardoso , Computer Methods in Biomechanics and Biomedical Engineering: Imaging & Visualization (2013): A 3D low-cost solution for the aesthetic evaluation of breast cancer conservative treatment, Computer Methods in Biomechanics and Biomedical Engineering: Imaging & Visualization, DOI: 10.1080/21681163.2013.858403

To link to this article: http://dx.doi.org/10.1080/21681163.2013.858403

Computer Methods in Biomechanics and Biomedical Engineering: Imaging & Visualization, 2013
http://dx.doi.org/10.1080/21681163.2013.858403

A 3D low-cost solution for the aesthetic evaluation of breast cancer conservative treatment

Hélder P. Oliveira[a]*, Jaime S. Cardoso[a], André T. Magalhães[b] and Maria J. Cardoso[c]

[a]*INESC TEC and Faculdade de Engenharia, Universidade do Porto, Porto, Portugal;* [b]*Faculdade de Medicina, Universidade do Porto, Porto, Portugal;* [c]*Breast Unit, Champalimaud Cancer Center, Champalimaud Foundation, Lisboa, Portugal*

(*Received 15 May 2013; accepted 20 October 2013*)

Breast cancer conservative treatment (BCCT) is now the preferred technique for breast cancer treatment. The limited reproducibility of standard aesthetic evaluation methods led to the development of objective methods, such as the software tool Breast Cancer Conservative Treatment.cosmetic results (BCCT.core). Although results are satisfying, there are still limitations concerning complete automation and the inability to measure volumetric information. With the fundamental premise of maintaining the system a low-cost tool, this work studies the incorporation of the Microsoft Kinect sensor in BCCT evaluations. The aim is to enable the automatic joint detection of prominent points, both on depth and RGB images. Afterwards, using those prominent points, it is possible to obtain two-dimensional and volumetric features. Finally, the aesthetic result is achieved using machine learning techniques converted automatically from the set of measures defined. Experimental results show that the proposed algorithm is accurate and robust for a wide number of patients. In addition, comparing with previous research, the procedure for detecting prominent points was automated.

Keywords: biomedical image processing; medical information system; image analysis

1. Introduction

Breast cancer is the most common cancer that affects women in the world. According to the most recent published data, breast cancer accounted for 23% (1.38 million) of the total new cancer cases and for 14% (458,400) of the total deaths by cancer in 2008 (Jemal et al. 2011). As 10-year survival from the disease now exceeds 80%, women are expected to live during long periods of time with the aesthetic consequences of the surgery and subsequent treatment. Therefore, a good aesthetic outcome is a fundamental issue in breast cancer treatment, being closely associated with psychosocial recovery and quality of life. However, it is known that a good aesthetic outcome is often difficult to achieve. In breast-conserving surgery, for example, approximately 33% of women will have a 'fair' or 'poor' aesthetic outcome (the two lowest grades in the Harvard scale – see below) (Pezner et al. 1985; Cardoso et al. 2006).

As far as treatment is concerned, it has progressed to the establishment of the breast cancer conservative treatment (BCCT) as an alternative to the classic mutilating mastectomy. Breast-conserving therapeutic approaches to breast cancer aim at obtaining local tumour control and survival rates equivalent to those achieved with the mastectomy procedure, but with better aesthetic results (Fisher et al. 2002; Veronesi et al. 2002). While the oncological outcome of breast conservation procedures can easily be assessed objectively, the cosmetic outcome has not yet an evaluation standard. Due to the diversity of procedures available in breast conservation, in both surgery and radiation therapy, various aesthetic results are expected. This makes it important to have an objective evaluation of the aesthetic results, to both assess and improve current strategies, as well as to identify variables that affect the final aesthetic result (Cardoso et al. 2012).

The aesthetic evaluation was initially carried out by one or more experts observing the patients directly or using photographic representations of them (Beadle et al. 1984). This evaluation was carried out using one of the existing scales that compare treated with non-treated breasts. The most widespread scale used until now for aesthetic evaluation of conservation breast procedures is the Harvard scale introduced by Harris et al. (1979). It classifies the overall cosmetic result according to four classes: Excellent (treated breast nearly identical to the untreated breast), Good (treated breast slightly different from the untreated breast), Fair (treated breast clearly different from the untreated breast, but not seriously distorted) and Poor (treated breast seriously distorted). However, it soon became clear that subjective evaluations had important limitations and disadvantages. For example, exemption is not always guaranteed since it is often carried out by professionals involved in the treatment (Beadle et al. 1984).

Objective methods were introduced in an attempt to overcome the lack of objectivity and reproducibility of subjective methodologies. Initial objective methods consisted in comparing the two breasts with simple

*Corresponding author. Email: helder.f.oliveira@inescporto.pt

measurements marked directly on the patients or on the photographs (Limbergen et al. 1989; Christie et al. 1996). In 2007, the Breast Cancer Conservative Treatment. cosmetic results (BCCT.core) software made possible to predict the global aesthetical result based on different individual characteristics semi-automatically and objectively extracted from frontal patient photographs (Cardoso and Cardoso 2007). The automation of the BCCT.core has been progressively improved. In Sousa et al. (2008), the breast contour is found using graph theory, based on the minimum cost path between previously known endpoints provided manually by the user. This line of work was improved in Cardoso et al. (2008), wherein additionally both the start and endpoints are found automatically. External endpoints are detected at the intersection of the arm contour with the trunk contour. However, this method depends strongly on the patient's arm position. When patients put their upper limbs down, the contour of the arm and trunk is overlapped, and thus it can be impossible to distinguish them. There are thus limitations on the complete automation of the BCCT.core – which is fundamental for high reproducibility – and the capability to extract volumetric information to improve the overall cosmetic evaluation. Other projects seem to be even more dependent on manual labour (Lee et al. 2012).

There are many advantages of using three-dimensional (3D) imaging as a tool for objective cosmetic evaluations: the breast can be viewed from a number of angles, estimating volume/volume deficit, and planning surgeries. With the development of the new oncoplastic methodologies in breast conservation, it is even more important to compare cosmetic results, helping tailoring the spectrum of techniques available to individual cases, without compromising either the oncologic or the cosmetic results (Asgeirsson et al. 2005). Several research groups have been making attempts with 3D technology. These approaches are based on 3D cameras (Moyer et al. 2008), 3D laser scanning (Eder et al. 2012) or even optoelectronic tracking systems (Catanuto et al. 2009). However, these require specialised hardware, software and personnel. The operation complexity and the high cost of this equipment make it difficult to use them on a daily clinical practice, which prevents their widespread use in the near future. Solutions in this area should remain affordable. Moreover, almost all currently used techniques based on 3D models do not try to predict the aesthetic result for a more informed choice of treatment, neither are they suitable to perform an automatic evaluation of the aesthetic result after surgery. Furthermore, 3D reconstruction of breasts is a very difficult task since the breast is featureless. For a survey on the methodologies used for the objective cosmetic evaluation, please refer to Oliveira et al. (2013). Recently, the Kinect (Microsoft Corp., Redmond, WA, USA) has been introduced as a promising low-cost and easy-to-use equipment for BCCT cosmetic evaluation (Oliveira et al. 2011, 2012). This tool can not only facilitate automation, but also provide volumetric information.

This paper extends the work for simultaneous extraction of breast contour and breast peak points (Oliveira et al. 2012), presenting a complete system assisting the aesthetical evaluation of BCCT, combining RGB (red, green, blue) and depth data acquired with the Kinect device. Contributions for detecting fiducial points, defining objective features and developing a new aesthetic model, are addressed in this study. The algorithms were developed to detect fiducial points without user intervention, and new models were created incorporating volumetric information. The prominent points were detected using synchronised depth and colour information.

The paper is organised as follows: Section 2 presents the main characteristics of the BCCT.core software. Section 3 introduces the main characteristics of the RGB-D devices, demonstrating their potential for aesthetic evaluation. The combination of RGB and depth data acquired with the Kinect device is addressed in Section 4. Here, it is demonstrated how the automation of fiducial points can be assisted by combining RGB and depth data, thus helping define 3D features (in Section 5) and the overall aesthetic evaluation (in Section 6). Section 7 presents the results of the experimental study. Finally, the conclusions are presented in Section 8.

2. BCCT.core design

The development of the BCCT.core entailed the semi-automatic extraction of several features from frontal images of patients (Figure 1), selecting the aspects with a higher impact on the overall cosmetic result: breast asymmetry, skin colour changes caused by radiotherapy treatment and surgical scar appearance. Afterwards, a support vector machine (SVM) classifier is applied to predict the overall cosmetic result from the recorded features (Cardoso and Cardoso 2007). The output of the BCCT.core is the categorisation of the aesthetic results of the BCCT into Excellent, Good, Fair and Poor classes (Harris et al. 1979).

The measurements are preceded by a semi-automatic localisation of fiducial points (nipple complex, breast contour and jugular notch of the sternum) on the digital photographs. The measurements are then based on these fiducial points. Measurements are automatically converted into an overall objective classification, using the SVM classifier, trained to predict the overall aesthetical result according to the Harris four-class scale.

2.1 Features

It is generally accepted within the scientific community that the overall aesthetic result after the BCCT is mostly

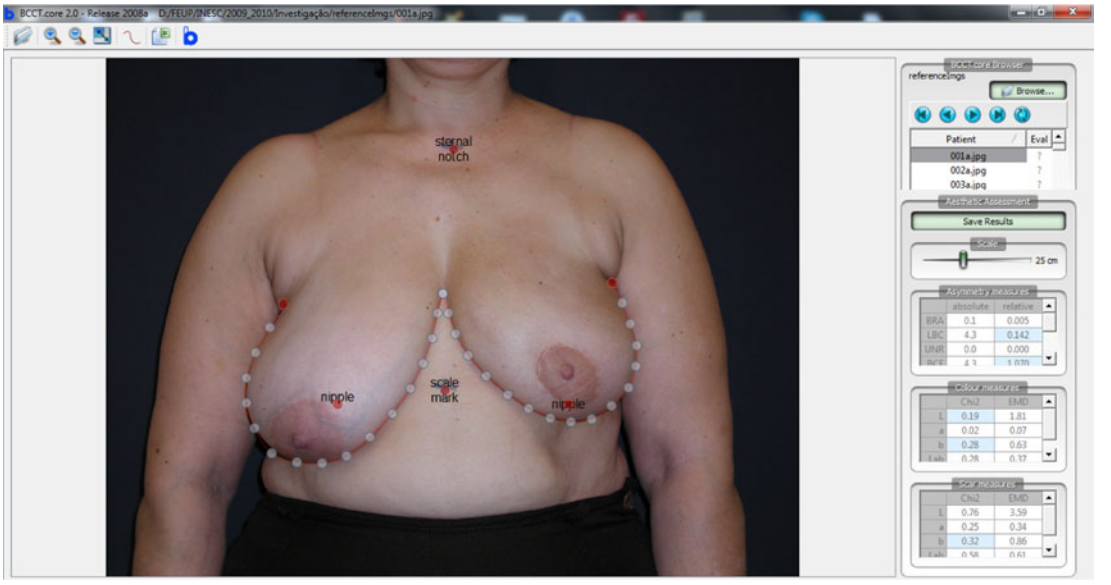

Figure 1. BCCT.core interface.

determined by changes in breast volume or shape (asymmetry) and visible alterations on the skin (Cardoso and Cardoso 2007). Skin changes are related to a disturbing surgical scar or radiation-induced pigmentation or telangiectasia.

In the BCCT.core, asymmetry is captured using 14 different indices. Seven of them require a scale correction between pixels measured on the digital photograph and the length in centimetres on the patient. The other seven indices are dimensionless, computed as the ratio of two lengths or areas. Skin colour changes, which are caused by radiotherapy treatment, were assessed by measuring the dissimilarity of the colour histogram of the two breasts using two different metrics: the χ^2 and earth mover's distance. The dissimilarity was computed using 3D histograms and on the histogram of each channel (RGB), amounting to eight different features recorded. The surgical scar appearance is translated into a localised colour difference. Each breast is divided into angular sectors, with the vertex on the nipple. For each sector, a colour histogram is computed and the similarity between corresponding sectors is measured according to the global colour change. In the end, eight different features are obtained from the maximum value of each pair of corresponding sectors.

2.2 The SVM classifier

SVMs have proved to be capable of representing complex classification or mapping functions. They find the representations using powerful learning algorithms. In this problem, there is an inherent ordering between the classes, which motivated the use of models especially designed for this kind of data. Using the data replication mapping for ordinal data in SVMs (Cardoso and daCosta 2007), and carrying out a simplified feature selection, the model is based on an SVM classifier with a radial basis function (RBF) kernel and requires only four features, two capturing asymmetry, one for skin colour changes and another for scar visibility (Cardoso and Cardoso 2007).

3. A kinect-based system for the aesthetic evaluation of BCCT

Over the last years, there have been dramatic improvements in the capabilities of RGB-D cameras, which provide both RGB and depth information in each image pixel (as in Microsoft Kinect). Combining depth and visual information brings new challenges and opens new possibilities in different fields of application, including medical applications. Several research communities have been making considerable progress in dealing either with 3D depth scans or with camera images; now it is time to take advantage of these advances and study the combination both of them.

This paper addresses the development of a Kinect-based system (BCCT.kore) to predict the overall outcome from data acquired with the Kinect (Figure 2). The proposed methodology requires (a) the automatic identification of fiducial points on the image, (b) suitable features must be chosen capturing the main factors (colour, shape, geometry, irregularity of the visual appearance of the treated breast) with an impact on the overall aesthetic result, finally, (c) it is necessary to find the optimum rule to map the individual features that will help make the overall decision.

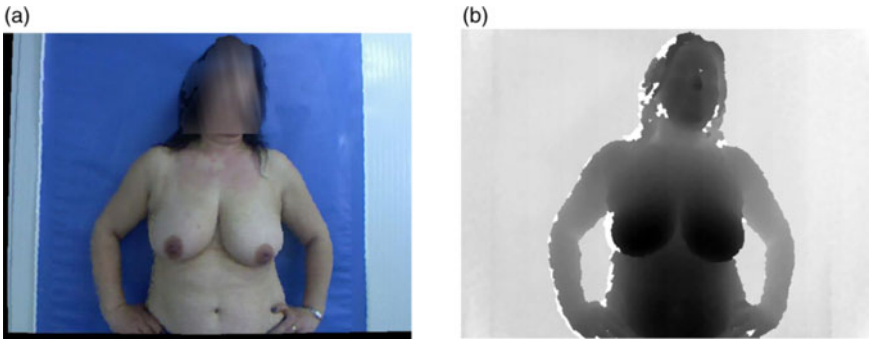

Figure 2. Microsoft Kinect data. (a) Patient photograph and (b) generated disparity map (normalised values).

It should be noted that in the Kinect, the colour sensor is separated and not synchronised with the depth sensor. Furthermore, it has a slightly wider field of view and is offset (by about 2 cm) from the depth sensor. Therefore, the RBG and range data are initially aligned using the methodology in Herrera et al. (2012).

3.1 Overview

The proposed system can be implemented as a sequence of a few high-level operations, as represented in Figure 3.

In the first step, the *breast peak* and *breast contour* are detected simultaneously based on the gradient vector flow theory and on a shortest path approach, respectively, in depth Kinect data. *Nipples* are detected based on the local invariant feature detectors theory, namely corner and regional detectors. Nipple detection is made using RGB Kinect data, assisted by the breast contour previously obtained. Next, *volumetric features* are defined over depth data, using all prominent points previously detected.

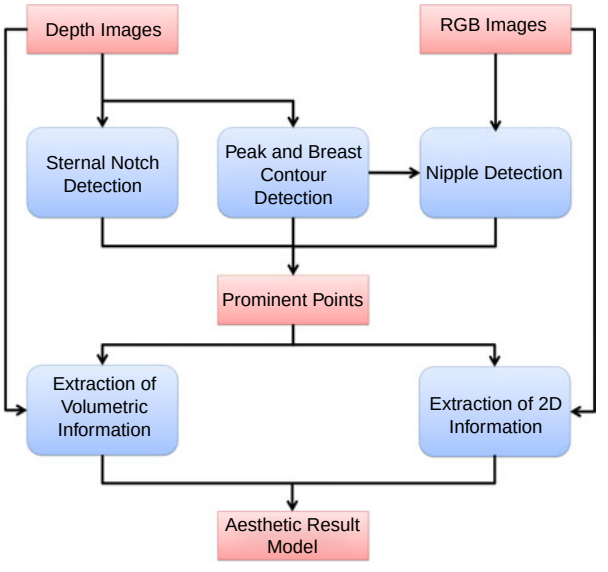

Figure 3. System flowchart for the joint RGB-D-based system.

Finally, using previous two-dimensional (2D) measurements (Cardoso and Cardoso 2007) and the new 3D features introduced in this work, a predictive model is built using a machine learning methodology to evaluate the overall cosmetic result. With the inclusion of measurements extracted from the 3D model, the global assessment result was improved over the 2D version in the BCCT.core without increasing complexity significantly.

First, it is necessary to provide an in-depth discussion on the automatic detection of prominent points since many of the novel aspects are present at this level.

4. A joint RGB-D-based detection of prominent points

4.1 Simultaneous detection of breast contour and breast peak points

Researchers are now paying more attention to the context to aid visual recognition processes. Context plays an important role in the human visual system recognition processes, and many important visual recognition tasks critically rely on context. Here, the mutual contexts of *breast contour* and *breast peak* (the area in the breast closer to the camera or further away from the chest wall, not necessarily the nipple) are modelled so that each one can facilitate the recognition of the other. When carried out independently, both tasks are non-trivial since many other parts of the image may be falsely detected. However, the two tasks can benefit greatly from serving as context to each other. To model the breast peak point, a filter is used to evaluate the degree of divergence of the gradient vectors within its region of support from a pixel of interest. The breast contour is modelled as a short path in a graph whose nodes correspond to the pixels on the image and the edges connect neighbouring pixels. The weight function on the edges is defined so that short paths correspond to paths that maximise the amount of gradient strength on the image along the path. The quality or probability of the joint model for the co-occurrence of breast peak and breast contour will be proportional to the individual qualities of

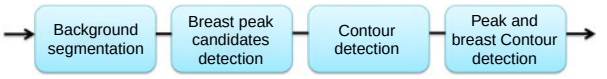

Figure 4. Algorithm flowchart for the simultaneous detection of breast contour and breast peak points.

the two parts. Next, the proposed algorithm is described in detail.

This process was implemented as a sequence of a few high-level operations over the depth information: (1) background segmentation, (2) breast peak candidate detection, (3) contour detection and (4) peak and breast contour decision (Figure 4).

Two simplifications were introduced with regard to the main steps presented above. First, the detection is carried out only over the patient's body, just to speed up the computation process. Second, the mutual detection of prominent points is addressed first by over-detecting peak candidates, and then by detecting contours using all peaks found.

As in other depth technologies, such as laser scanners or range finding cameras, the Kinect's output contains a large amount of missing data and noise as a result of occlusions. These undesirable conditions are typically represented as white pixels (Figure 2(b)). These missing values were excluded from all of the following operations. The remaining pixels were scaled between 0 and 1. Finally, a 3×3 smooth filter was applied to eliminate noise resulting from the acquisition process. Figure 5(c), (d) shows the output of this pre-processing task.

4.1.1 *Adaptive background segmentation*

Acquisitions were mainly carried out in a uniform background. However, occasionally the background is cluttered with the presence of different objects at different depths. Objects can appear at depths similar to the patients', or just the different body parts at different depths, dismissing the application of traditional thresholding methods such as Otsu's (Figure 5(c)). In this work, it was considered that the patient is at a somewhat central position on the image and is likely the 'object' closer to the camera.

This property was exploited using a density image defined by transforming the depth information on the XY plane (D) to the XZ plane (Φ) (Kim and Park 2004). The value at position (x, z) of the density image denotes the number of points at depth z in column x of the depth image (by counting along the Y direction) (Figure 5(a)).

$$\Phi(x, z) = \sum_{y=1}^{n} D(y, x) \quad \text{where} \quad D(y, x) = z. \tag{1}$$

Intuitively, each column of the density image is the histogram of the corresponding column in the depth image. A global thresholding method of the original XY image corresponds to a horizontal line in the XZ image, differentiating background from foreground (Figure 5(a), (c)). A more adaptive method is allowing the threshold to vary from column to column. Since it is not expected that the threshold will change significantly between consecutive columns, the method can be constrained to enforce this

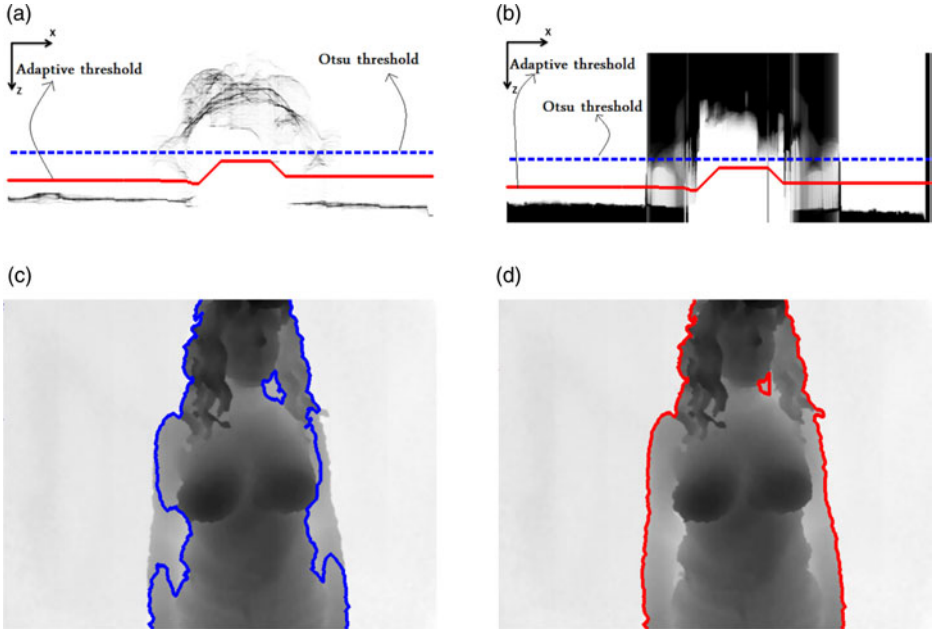

Figure 5. Adaptive background segmentation. (a) XZ plane depth information; (b) XY variance plane; (c) Otsu's segmentation and (d) adaptive segmentation.

knowledge. The constrained adaptive thresholding leads to a continuous curve in the *XZ* image from left to right.

The constrained thresholding can be easily tackled using graph-based concepts. For that, the quality (cost) of each candidate threshold needs to be estimated; in the resulting cost image (interpreted as a graph), the computation of the shortest path between left and right margins yields the individual thresholds (Figure 5(d)).

In our application scenario, the information along each column can present one of three different patterns: (1) background only, (2) 'object' and background and (3) 'object' only. The cost will be set according to an initial estimate of the column pattern. The specific patterns are predicted by analysing the mean and the variance of a Gaussian distribution $\mathcal{N}$ fitted to *XZ* data (Φ). Table 1 shows the qualitative indication of the values expected for each pattern type.

Furthermore, for each depth z and position of column x, the variance above: Var_a (the variance in the column x of the depth values greater than z) and the variance below: Var_b (the variance in the column x of the depth values less than z) are computed. The cost for each possible threshold is then set by the following rule, according to the predicted pattern: (pattern 1) cumulative value of the minimum of the variance ($\mathrm{Var}_{\mathrm{min}}$) from 1 to Nbins; (pattern 2) average of the two variances ($\mathrm{Var}_{\mathrm{mean}}$); (pattern 3) cumulative value of the minimum of the variance ($\mathrm{Var}_{\mathrm{min}}$) from Nbins to 1 (Figure 5(b)).

$$\mathrm{Var}_{\mathrm{min}}(x,z) = \min(\mathrm{Var}_a(x,z), \mathrm{Var}_b(x,z)), \tag{2}$$

$$\mathrm{Var}_{\mathrm{mean}}(x,z) = \frac{\mathrm{Var}_a(x,z) + \mathrm{Var}_b(x,z)}{2}. \tag{3}$$

Table 1. Fitting parameters.

Pattern	$\mathcal{N}(\sigma^2)$	$\mathcal{N}(\mu)$
(1)	Low	High
(2)	High	High and low
(3)	Low	Low

4.1.2 *Breast peak candidate detection*

The breast peak is modelled using a filter that evaluates the degree of divergence of the gradient vectors from a pixel of interest. A major benefit of using depth-map images is the high contrast observed in the breast area. The peak point of the breast corresponds to the point in the breast where disparity attains the lowest value. The typically round or tear drop shape of a breast leads to a distinctive pattern in the gradient vector field, where the gradient diverges in all directions (Figure 6 shows a toy example).

Breast peaks (Figure 7(a)) are detected using an approach similar to the convergence index filter (Kobatake and Hashimoto 1999), in which the image is filtered with a radial vector field pattern, as presented in Figure 7(b).

Gradient $g(x,y)$ is computed first by calculating the horizontal G_x and vertical G_y components of the image gradient. In this work, a Gaussian filter was applied, and only the gradient orientation angle $\theta(x,z)$ was used by previously normalising the norm of the gradient vectors to unity.

$$\theta(x,z) = \tan^{-1}\frac{G_y}{G_x}. \tag{4}$$

The similarity between the template and the image was assessed using two different measurements:

- Cross-correlation

$$(f*g)[\mathbf{n}] \stackrel{\mathrm{def}}{=} \sum_{\mathbf{m}} f^*[\mathbf{m}]g[\mathbf{n}+\mathbf{m}], \tag{5}$$

  where f and g represent the gradient orientation vector field and the template vector field, respectively. f^* denotes the complex conjugate of f.
- Circular correlation, introduced by Fisher and Lee (1983).

The result of cross-correlation and circular correlation, with regard to Figure 6(a), can be graphically represented as shown in Figure 8, where the values range from -1 to 1, with -1 represented in blue and 1 in red.

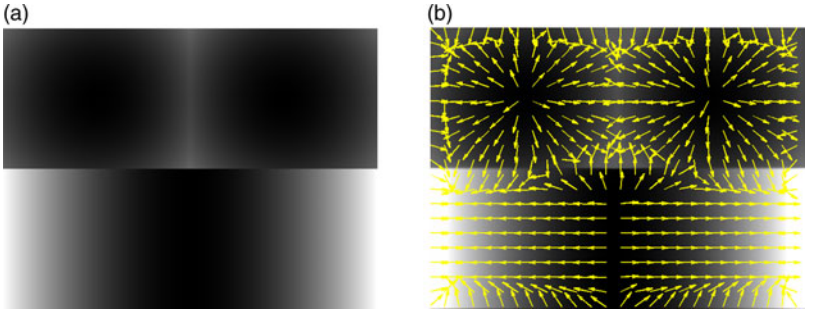

Figure 6. Toy example of different gradient shapes. (a) Disparity example and (b) gradient vector field from toy example in (a).

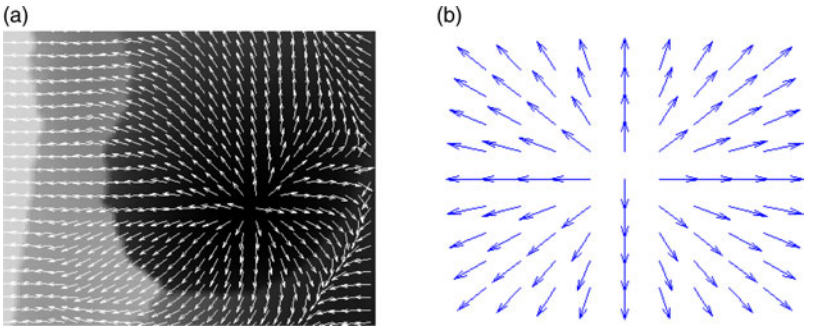

Figure 7. Breast peak candidate detection. (a) Breast gradient vector field (five-pixel spacing) and (b) template vector field. (The magnitude of the vectors is normalised.)

Breast peak candidates correspond to all local maximum positions.

4.1.3 *Contour detection*

Breast contour detection was modelled using a shortest path in a graph whose nodes correspond to the pixels on the image and the edges connect neighbouring pixels, an approach that is similar to Cardoso et al. (2008) and Oliveira and Cardoso (2009). Breast boundary can be seen as a change in the grey-level values of the pixels, originating an edge in the resulting image. Interpreting the image as a graph with pixels as nodes and edges connecting adjacent pixels, the low-cost path through edge pixels corresponds to the breast contour, using an appropriate weight function.

Since the breast contour is approximately circular and centred on the breast peak candidates, the computation is more naturally carried out by adopting polar coordinates, with the origin of the coordinates in the peak candidate. The shortest path is computed using dynamic programming to increase efficiency. Formally, let I be an $N_1 \times N_2$ image and define an admissible path as:

$$\mathbf{s} = \{(x, y(x))\}_{x=1}^{N_1}, \text{ s.t. } \forall x |y(x) - y(x-1)| \leq 1,$$

where y is a mapping $y : [1, \ldots, N_1] \rightarrow [1, \ldots, N_2]$.

This means that an admissible path is an eight-connected path of pixels on the image from left to right, containing only one pixel in each column of the image. The first step is to traverse the image from the second column to the last and to compute the cumulative minimum cost C for all possible connected staff lines at each entry (i, j):

$$C(i,j) = \min \begin{cases} C(i-1, j-1) + w(p_{i-1,j-1}; p_{i,j}), \\ C(i-1, j) + w(p_{i-1,j}; p_{i,j}), \\ C(i-1, j+1) + w(p_{i-1,j+1}; p_{i,j}), \end{cases}$$

where $w(p_{i,j}; p_{l,m})$ represents the weight of the edge incident with pixels at positions (i, j) and (l, m).

At the end of this process,

$$\min_{j \in \{1, \ldots, N_2\}} C(N_1, j)$$

indicates the end of the minimal connected path. Hence, in the second step, one backtrack from this minimum entry on C is applied to find the optimal path.

Each column in the polar image corresponds to the derivative along each radial line in the original space:

$$G_\theta(r) = \frac{f(r+h) - f(r-h)}{2h},$$

where $h = 1$ and r is the radius.

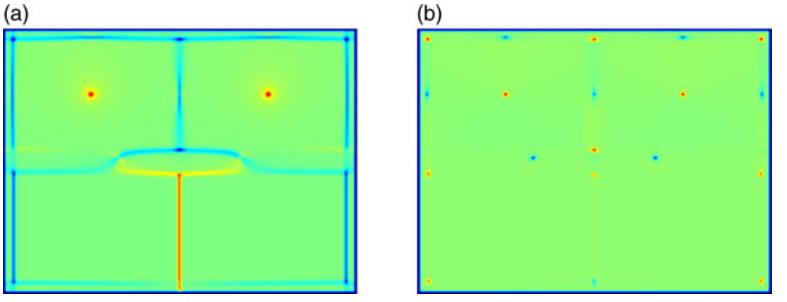

Figure 8. Graphical demonstration of correlation approach. (a) Cross-correlation result and (b) circular correlation result.

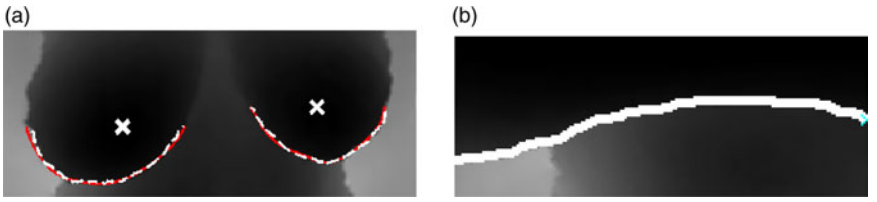

Figure 9. Brest contour detection. (a) Breast contour – ground truth (solid red line), detected (dashed white line) and (b) polar image and detected contour (white line).

Each four-neighbour pixel arc is weighted by the following exponential law:

$$f(g) = f_l + (f_h - f_l)\frac{\exp(\beta(255 - g)) - 1}{\exp(\beta 255) - 1,}$$

where $f_l, f_h, \beta \in \Re$ and g is the minimum of the gradient computed for the two incident pixels. The numerical factor 255 corresponds to the maximum value taken by $G_\theta(r)$, which is in the range of $[0; 255]$. For eight-neighbour pixels, the weight was set to $\sqrt{2}$ times that value. The parameters f_l, f_h and β were fixed at $f_l = 2$, $f_h = 128$, $\beta = 0.0208$. This cost function and parameters were optimised in a previous work (Oliveira and Cardoso 2009).

Since the start and the end of the breast contour are unknown, at this phase a conservative approach is used, searching only for angles between π and 2π (Figure 9(a)). Later on, the contour will be completed. The candidate contour is then the output of the shortest path algorithm in the polar image (Figure 9(b)).

4.1.4 *Peak and breast contour decision*

The quality or probability of the joint model for the co-occurrence of breast peak and breast contour is computed maximising the joint probability of the individual parts. It is assumed that the joint probability is a monotone function of the product of the correlation outputted by the divergence filter ρ_p and the quality of the detected contour $\mu(\Delta C)$. The quality of the contour $\mu(\Delta C)$ is evaluated as the average magnitude of the directional derivative along it and ρ_p is the cross-correlation or circular correlation of the centre candidate. Therefore, the final decision consists in selecting the pair (peak, contour) that maximises the quality measurement:

$$Q(Cp) = \mu(\Delta C) \cdot \rho_p. \tag{8}$$

Taking advantage of body symmetry with regard to the sagittal plane, a pair (peak, contour) was selected for the right and another for the left of the body centre of mass. The centre of mass is computed using the patient body mask obtained in Section 4.1.1.

4.1.5 *Complete breast contour detection*

The complete detection of the breast contour is an extension of the methodologies presented in Section 4.1.3. The algorithm is divided into the following operations: (a) defining contour endpoints and (b) defining contour between detected endpoints.

Although the definition of the external endpoints is not consensual, even among the medical community, the position of the external endpoints can be assumed to be at the point of the body where the arm contour intersects the trunk contour. However, when the patient's arms are alongside the body, the arm's contour is almost indistinguishable from the trunk's contour. Therefore, the aim was to find the external endpoint by simply measuring the 'strength' of vertical edges in the external boundary of the breast. External endpoints are detected with the following operations:

(1) Computing horizontal derivative.
(2) Extracting vertical edges with an appropriate threshold (experimentally tuned).
(3) Detecting connected components.
(4) Extracting extremities from connected components.
(5) Obtaining contour endpoints from detected extremities.

After detecting all extremities from vertical edges, the outer contour endpoint is defined as the closest extremity to the endpoint obtained during the partial contour detection phase, presented in Section 4.1.3 (Figure 10). These operations were carried out separately for each breast according to the sagittal plane defined previously.

The internal endpoint of each breast contour is defined during the complete contour detection. This task was carried out following the theory presented in Section 4.1.3 with the following constraints: the starting point contour is defined as the external endpoint detected previously; and the search for the internal endpoint is limited to the sagittal plane or to the horizontal plane equidistant to the horizontal planes defined by the two external endpoints (Figure 10).

In conclusion, the internal endpoints are obtained by intersecting each breast contour and the sagittal plane or the average horizontal plane defined by the external endpoints.

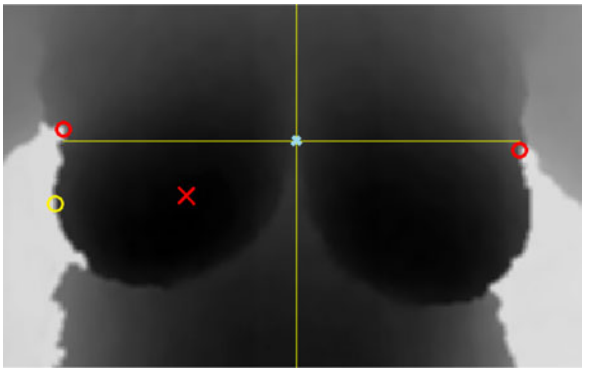

Figure 10. Complete contour detection and internal endpoint definition – external endpoint detected (red circle) – previous outer endpoint (yellow circle) – breast peak point (red cross).

4.2 *Sternal notch detection*

The jugular notch is a visible dip found at the superior border of the manubrium of the sternum, between the clavicular notches. To automatically detect the sternal notch (ST), it is necessary to locate the midpoint of the upper portion of the region at the intersection of the neck and the torso. To determine the point where the torso intersects with the neck, the depth values are projected (summed) along the rows image (Figure 11).

The graph from the horizontal projection presents a characteristic shape. Specific parts of women's bodies can be found by detecting local minima (green ∗) and maxima (red ∗). The ST (*local maximum*)/chest (*local minimum*) pair is the pair of consecutive maximum and minimum at the highest distance, yielding the location of the ST (blue circle).

4.3 *Nipple detection*

The nipples were detected using RGB images and the delimitation of breast contours previously carried out in the depth images was taken into account, which obviously simplifies the process.

The breast surface is generally characterised as a featureless shape, and typically the nipple is the most prominent feature. However, many other features can be mistaken for the nipple when using traditional feature detectors based on colour or more complex features such as texture. Since the nipple is part of the areola complex, a closed region enclosing the nipple, regional information can make it easier to detect the nipple. We start by over detecting nipple candidates; then, *one or more* closed contour(s) were found enclosing each candidate. Finally, the best pair (candidate/closed contour) was selected combining information from the contour and the nipple candidate.

The areola complex is typically more textured than the rest of the breast surface. Therefore, a corner-based method was applied to detect the nipple. However, it was quite difficult to achieve a good detection rate without detecting multiple spurious points; controlling the spurious points leads to a high miss detection rate. Therefore, a corner descriptor (Harris detector) is used as an initial step by over detecting possible nipple locations (Figure 12(a)). Afterwards, using nipple candidates, a circular window is centred on each candidate in order to find the areola contour. Using polar coordinates and the methodologies presented in Section 4.1.3, a closed path (starting and ending on the same row of the polar image)

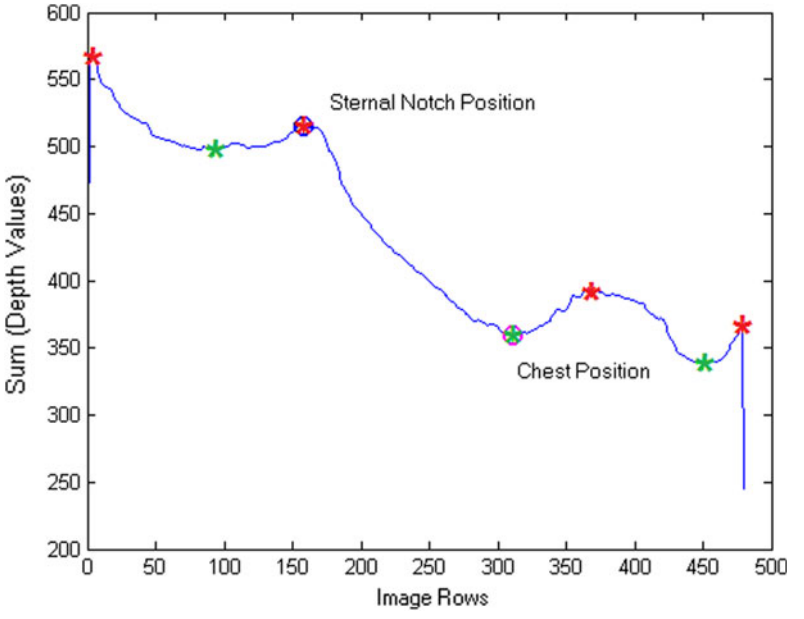

Figure 11. Sternal notch detection (red ∗ – local maximums; green ∗ – local minimums; blue circle – ST position; magenta circle – chest position).

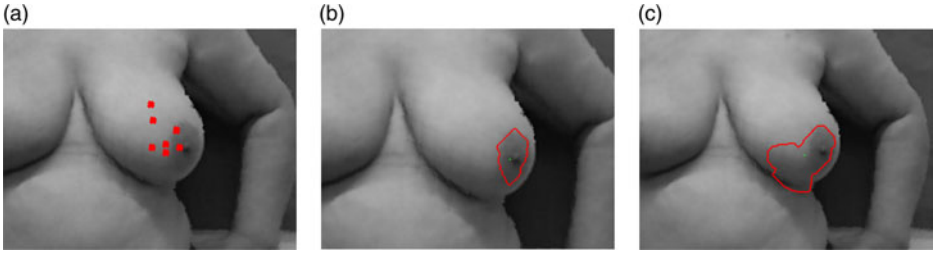

Figure 12. Nipple detection. (a) Harris corner detection inside the breast; (b) areola detection (true corner) and (c) areola detection (false corner).

was computed (Figure 12(b),(c)). Since the areola complex is often rich in edges and false contours, the algorithm was implemented to produce all closed contours found in the process. Note that the method adopted (Monteiro et al. 2013) to find the best closed contour may end up finding multiple closed contours. Instead of just keeping the closed contour with the smallest cost, all of them are kept to carry out a joint analysis of the contour features (such as shape) and centre candidate. This approach has two main assumptions: first, at least a nipple candidate lies within the true areola contour; second, the areola contour represents a closed path over strong gradient pixels. The areola contour is not necessarily circular and the candidate nipple does not need to match the true position of the nipple to correctly detect contour.

After completing these two steps, several (nipple candidate/areola contour) pairs are detected. The challenge now is to discriminate the correct candidate/contour pair. A combination of several features and a classifier-based approach was implemented. The extracted features include the following:

- The Harris corner quality factor, ρ_h.
- The average magnitude of the directional derivative of the areola contour, $\mu(\Delta C_a)$.
- The shape factor of the contour, S_a.
- The equivalent diameter of the contour, d_a.

The Harris corner quality factor ρ_h measures the confidence of the detector in the corner or junction found. The average derivative $\mu(\Delta C_a)$ measures the magnitude (strength) of the directional derivative over the areola contour; the circularity of the contour is measured by the shape factor S_a:

$$S_a = \frac{4\pi A}{P^2}, \tag{9}$$

where P is the perimeter and A is the area enclosed by the contour. The shape factor takes values in the interval $[0, 1]$, where 1 represents a perfect circle. The equivalent diameter d_a represents the diameter of a circle with the same area as the inner contour region.

Classification methods based on SVM classifiers were adopted, using the popular LIBSVM (Chang and Lin 2011) implementation and a probability estimation approach.

5. Volumetric feature definition

Previous techniques to evaluate the cosmetic result are based on measurements taken from representative frontal photographs of the patients, being therefore limited by the information present in the frontal view. Besides the appearance of the surgical scar and the skin colour change induced by radiotherapy, the measurements are mostly based on asymmetries between the breasts.

The use of volumetric data enables a more complete understanding and reliable aesthetic assessment. Nevertheless, the volumetric features must be objectively and consistently processed, a requirement for a reproducible assessment. In this work, the 30 features extracted from the frontal view in the BCCT.core (Cardoso and Cardoso 2007) are complemented with volume, surface area, nipple height and 3D nipple retraction assessment (3DNRA) measured in the 3D information taken from the Kinect.

Instead of limiting any subsequent analysis to an initial choice of a volumetric feature, it was decided to record multiple indices (some of which already introduced in the literature (Eder et al. 2012) with the purpose of proceeding later to a feature selection process. The measurement of the volumetric features relied on the prominent points detected as reported previously (Section 4). The indices recorded to assess volumetric information were the following:

- Volume difference assessment (VDA): quantifies the ratio of the total volume between the two breasts. The volume is defined as the sum of voxels (unit values) between the estimated body plane and the breast surface (Figure 13(a) – red blocks).
- Surface area assessment (SAA): quantifies the ratio of the surface area between the two breasts. To compute the area of a surface, it is necessary to compute the area of each rectangular face of the surface and then put them together (Figure 13(a) –

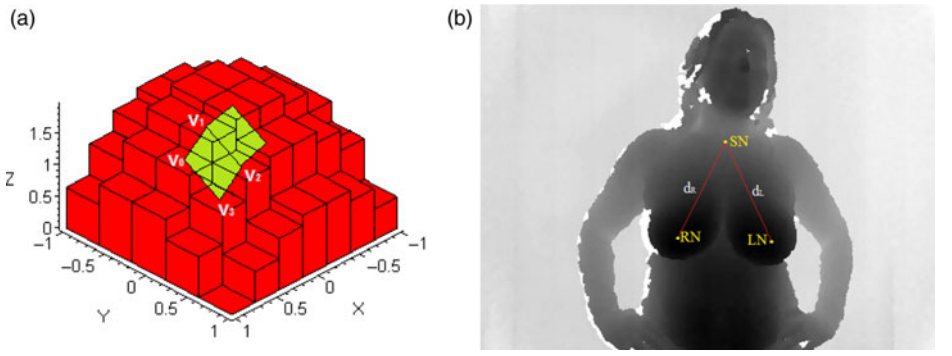

Figure 13. (a) Illustration of VDA and SAA measurement based on voxels and (b) illustration of 3DNRA measurement.

green rectangular faces). To compute the area of each rectangular face, it is convenient to imagine the face as being split into two triangular pieces. The cross product can be used to compute the area of a triangle in a 3D space. If the coordinates of the vertices are given $v_i = (X_i, Y_i, Z_i)$, then the surface area A_s is computed as:

$$A_s = 0.5 \cdot |(v_2 - v_1) \times (v_3 - v_1)|. \quad (10)$$

- Nipple height assessment (NHA): quantifies the ratio of the nipple height between the two breasts. The nipple height is defined by measuring the distance (in depth) between nipple and chest position.
- 3DNRA: quantifies the ratio between the retraction of the two nipples. The nipple retraction index is computed based on the 3D information of three fiducial points: right nipple, left nipple and the ST (Figure 12). The 3DNRA is the ratio of the 3D Euclidean distance between the nipples and the ST.

Three of the features considered (volume, surface area and nipple height) have to take the chest wall plane (inter mammary fold) as reference. The chest wall plane is considered to be parallel to the camera plane at the minimum depth that is found in the area between the inner breast contour extreme points and the lowest bottom point of the breasts.

6. Aesthetic model

The problem addressed here, which deals with predicting the overall Harris score, involves classifying examples into classes that have a natural order. Therefore, techniques were used which are specifically designed for that purpose (Cardoso and daCosta 2007) instantiated in SVMs. Two schemes were investigated to integrate 3D and 2D features. The first approach is based on a typical scheme in which 2D and 3D features are combined in a simple vector without any restriction. A classifier is then trained on this enlarged vector. A second approach is based on a cascade scheme (Gama and Brazdil 2000); here, the output of the model based on 2D features is used only as input together with the 3D features for a second model (Figure 14).

7. Results

The proposed system was evaluated in a database comprising data from 131 patients. All patients were treated with conservative breast surgery, with or without auxiliary surgery, and with whole breast radiotherapy, with treatment completed at least one year before the onset of the study. The acquisition of pictures in medical environment is not always easy to carry out. Patients must agree with the process, and sometimes doing that on a voluntary basis makes it difficult to increase the number of cases in the database. For each patient, the data included multiple depth and colour frontal images acquired with the Kinect. The height of both nipples (distance between the medial projection of the nipple and the sternum measured with two rulers) was manually obtained by the physician during the acquisition period and included in the database.

Manual ground truth annotation was carried out for the Kinect data. The position of the breast peaks and the breast contours was annotated in depth-map images; the nipples and suprasternal notch were annotated in the Kinect colour

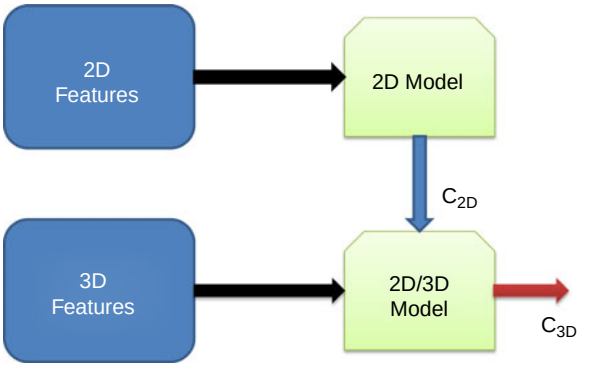

Figure 14. Cascade classifier flowchart.

Table 2. Breast peak point detection error (in mm).

		Standalone		Simultaneous detection	
Metric	Breast	$\mu(\sigma)$	# Miss (%)	$\mu(\sigma)$	# Miss (%)
Circ. corr.	Right	23.46 (67.03)	73 (7.50)	13.06 (44.76)	27 (2.77)
	Left	14.81 (34.84)		9.03 (20.14)	
Cross-corr.	Right	15.70 (49.14)	43 (4.41)	6.42 (4.39)	0 (0.00)
	Left	11.32 (25.52)		6.33 (3.74)	

image. A subjective evaluation of the overall aesthetic result is also provided based on the Harvard scale.

7.1 *Breast peak detection*

Breast peak detection was evaluated in 487 depth-map images from 131 patients. The accuracy of breast peak point detection was measured using the Euclidean metric distance (Table 2).

The first column (standalone) shows the detection error that would be obtained by making the decision based on maximising the output of the convergence filter. The second column (simultaneous detection) depicts the performance for the proposed scheme. Miss detection means that breast peak point was detected outside the breast area. Therefore, using context in this task is clearly advantageous. Moreover, cross-correlation attains better results both in the mean error and in the miss detection, with an average error of 6.38 mm. Some results using simultaneous detection and cross-correlation are shown in Figure 15.

7.2 *Breast contour endpoints detection*

Breast contour endpoints detection was also evaluated in 487 depth-map images. The endpoint detection accuracy was measured using the Euclidean metric distance (Table 3).

The average error of 12.6 mm is a consequence of the ambiguity of the endpoint concept. Nevertheless, as will be presented next, the impact on the remaining tasks is low. Some results for the contour endpoints detection are shown in Figure 16.

7.3 *Breast contour detection*

The breast contour detection error using the joint model for the co-occurrence of breast peak and breast contour was evaluated based on the Hausdorff and average distances (Table 4). The direct Hausdorff distance between two sets of points A and B is defined as:

$$h(A,B) = \max_{a\in A} \min_{b\in B} \|a-b\|, \tag{11}$$

where $\|\cdot\|$ is the Euclidean distance. The motivation for using this metric is that it represents the worst case scenario. As in the previous steps, breast contour detection was evaluated in 487 depth-map images.

From Table 4, it is possible to observe that the proposed algorithm presents a very interesting performance. The average error is quite low, around 3 mm. It represents the result after the two phases of the algorithm: contour endpoint detection and complete contour definition. Although a relatively high error is found on the location of the endpoints, the breast contour algorithm recovered the correct contour rapidly, thus obtaining a lower average error and a high Hausdorff distance. Some results for the complete contour detection are shown in Figure 17.

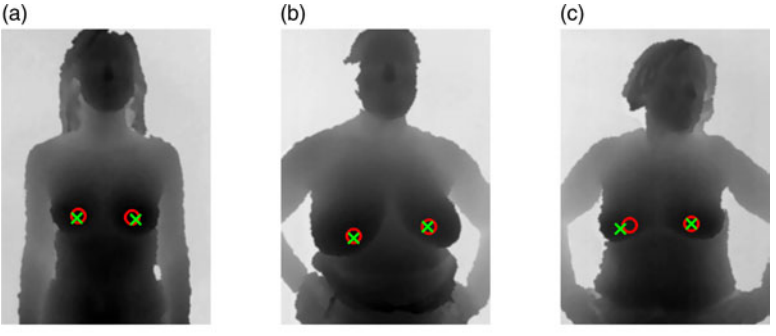

Figure 15. Breast peak detection examples. Detected breast peak (red circle) – ground truth breast peak (green cross).

Table 3. Endpoint detection error (in mm).

Breast	End point	$\mu(\sigma)$
Right	Outer	11.89 (12.21)
	Inner	13.21 (11.52)
Left	Outer	11.93 (11.74)
	Inner	13.34 (10.26)

7.4 Nipple detection

A training set to design a binary classifier was built by manually labelling all pairs of candidate/contour detected in a set of 76 images (yielding 1740 candidate/contour pairs). An SVM classifier was optimised by carrying out a grid search on the parameters of the model (*C* parameter, degree of the polynomial kernel and bandwidth of the RBF kernel) using cross-validation with fourfolds. Finally, the performance of the model was estimated in a test set composed of 248 colour images. When more than one nipple/contour pair is predicted as positive in an image, the prediction with the highest probability is selected (SVMs were implemented with LIBSVM (Chang and Lin 2011), enabling the estimation of the probability).

The performance in the test set, presented as the average distance between the manually marked nipple and the predicted nipple, using the best subset of features, is summarised in Table 5. 'Miss detection' means that the nipple was detected outside the areola. The table includes

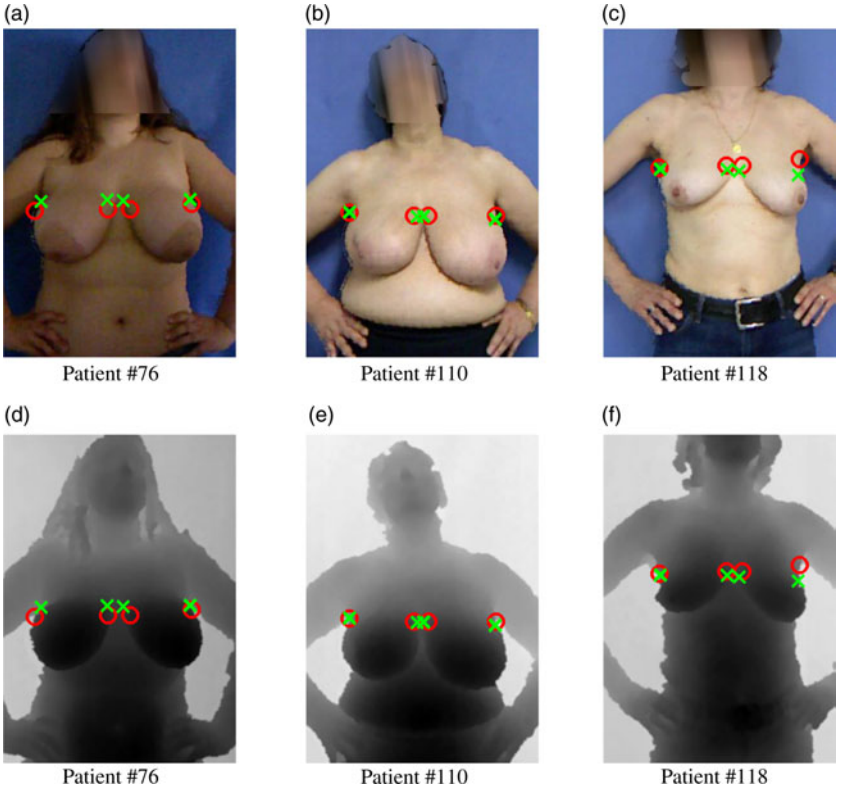

Figure 16. Contour endpoints detection examples. Detected endpoints (red circle) – ground truth endpoints (green cross).

Table 4. Breast contour detection error (in mm).

	Detected ⇒ ground truth				Ground truth ⇒ detected			
	Right breast		Left breast		Right breast		Left breast	
	Mean	Max	Mean	Max	Mean	Max	Mean	Max
Average	3.26	14.12	3.18	12.53	2.92	14.08	2.82	12.23
St. dev.	1.81	10.52	2.14	10.19	1.69	9.23	2.08	9.80
Max	23.88	63.21	22.13	81.70	23.75	60.93	18.49	101.05
Min	1.27	3.94	1.14	3.63	0.99	3.12	1.00	2.83

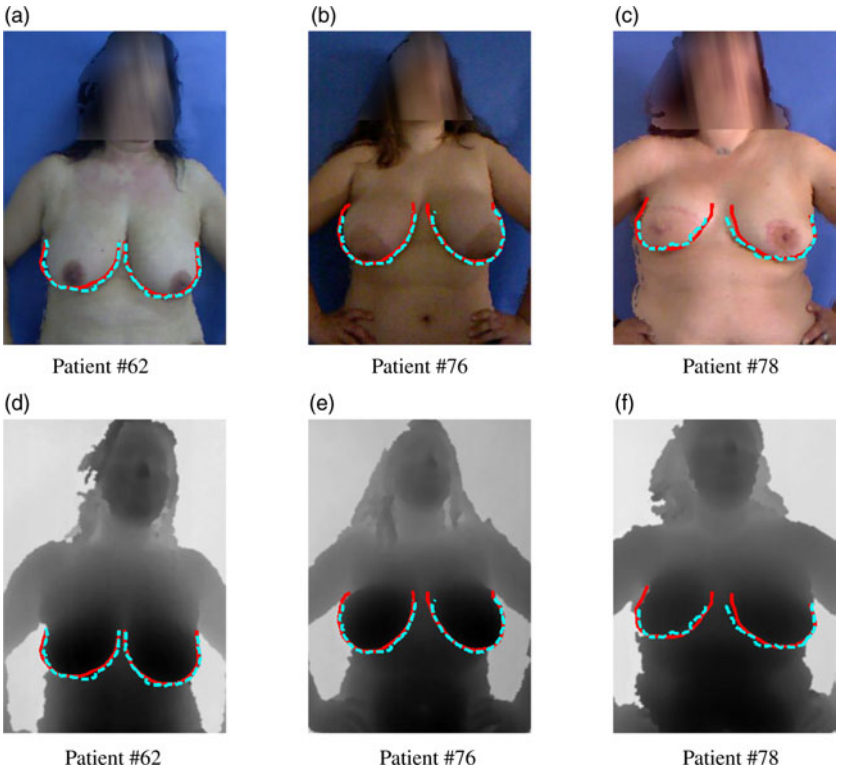

Figure 17. Complete contour detection examples. Detected contour (dashed cyan line) – ground truth contour (solid red line).

the results for the best parameterisation of each kernel, and for different subsets of features. The best results show an average error around 6 mm and a single detection outside the areola complex.

Some results for the nipple detection are shown in Figure 18.

Table 5. Average distance between the manually marked nipple and the predicted nipple in cm (results are present in the format 'mean (standard deviation)') and MER.

Features/kernel (parameters)	Linear – $\mu(\sigma)$ # Miss (%)	Polynomial Degree (2) $\mu(\sigma)$ # Miss (%)	RBF Gamma (1) $\mu(\sigma)$ # Miss (%)
$\{S_a\ \mu(\Delta C_a)\}$	0.80 (1.00) 26 (5.66)	0.78 (0.95) 24 (5.23)	0.79 (0.92) 27 (5.88)
$\{S_a\ \rho_h\}$	0.84 (1.08) 41 (8.93)	0.73 (0.85) 25 (5.45)	0.84 (1.00) 35 (7.63)
$\{S_a\ d_a\}$	0.92 (1.40) 40 (8.72)	0.92 (1.41) 39 (8.50)	0.89 (1.35) 37 (8.06)
$\{S_a\ \mu(\Delta C_a)\ \rho_h\}$	0.77 (0.96) 35 (7.63)	0.65 (0.62) 11 (2.40)	0.80 (0.92) 31 (6.75)
$\{S_a\ \mu(\Delta C_a)\ d_a\}$	0.74 (1.00) 19 (4.14)	0.65 (0.66) 10 (2.18)	0.65 (0.65) 12 (2.61)
$\{S_a\ \rho_h\ d_a\}$	0.79 (1.15) 25 (5.45)	0.65 (0.69) 11 (2.40)	0.74 (0.84) 23 (5.01)
$\{S_a\ \mu(\Delta C_a)\ \rho_h\ d_a\}$	0.74 (1.00) 24 (5.23)	0.64 (0.62) 16 (3.49)	0.61 (0.47) 1 (0.22)

7.5 *Nipple height assessment*

This section presents a direct evaluation of the nipple height feature (based on the ratio between the treated and the untreated breast) by comparison with the measurement taken by the physician. Due to the absence of a ground truth, the quality and effectiveness of the other features (volume, surface and 3D nipple retraction) will be evaluated indirectly in Section 7.6 through the improvements to the final overall aesthetic evaluation.

Since it is a time consuming process, the measurements made by the physician are available only for a subset of 65 patients from the initial database. Figure 19 presents a comparison between the ratios detected automatically and the ground truth ratios for the nipple height feature.

The ratios detected automatically are very similar to those obtained by the physician, with a correlation of 0.92. Aspects that can interfere with the data quality include smaller patient breasts or similar breast shapes. It is also important to highlight that the physician also introduces errors during the manual measurement. A proper correlation gives further support to the use of the Kinect in cosmetic evaluations, facilitating its acceptance by clinical experts.

7.6 *Aesthetic evaluation*

Before designing a new model, it was necessary to select the set of features to be used in the study. The selection of

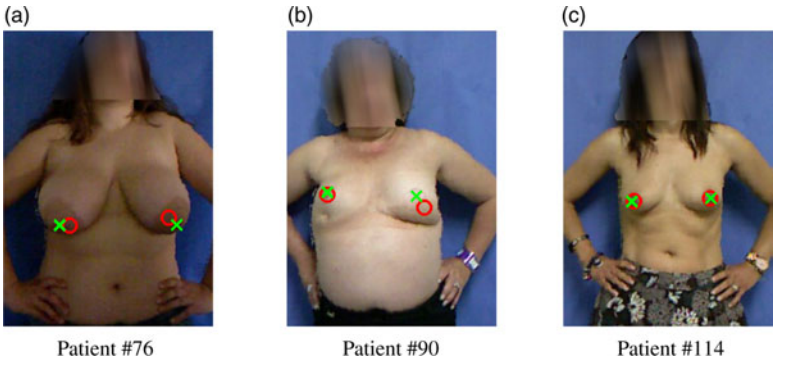

Figure 18. Nipple detection examples. Detected nipple (red circle) – ground truth nipple (green cross).

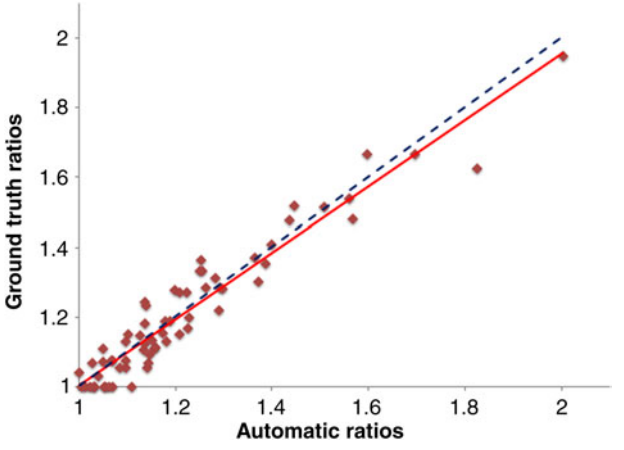

Figure 19. Scatter plot of depth height ratios. The red line is the trendline for graph data. The blue dashed line represents the ideal trendline.

2D features was based on previous studies (Cardoso and Cardoso 2007; Oliveira et al. 2010), whereas the 3D features were those presented in this work.

The model was designed using the selected features, considering all the possible subsets, using a leave-one-out scheme (Duda et al. 2000). The subjective evaluation carried out by the physicians was used as reference to train the models. Since the two experts did not reach consensus, the evaluation was carried out separately for each of the physicians. Models considering three and four classes were developed for the first physician evaluation, while for the second physician the evaluation was only carried out with three classes due to the lack of patients evaluated as 'Poor'. Taking into account previous work on the same problem, the SVMs proved to be a suitable solution, mostly due to the limited amount of data available (Cardoso et al. 2005a, 2005b). Linear and RBF kernel were tested, carrying out a 'grid-search' on the parameters of the models (h and s parameters of the data replication method were left constant at 1 and 2, respectively). Exponentially growing sequences of C were tested: $C = 2^0, 2^2, 2^4, 2^6$, while γ, for the RBF kernel, was tested with: $\gamma = 0.125, 0.25, 0.5$.

The test results concerning the misclassification error (MER), the correlation (Corr) and Kappa statistics for the first ranked feature subset are summarised in Table 6 for 2D features, Table 7 for the cascade scheme and Table 8 for the non-restricted scheme, which combines 2D and 3D features. The discrimination of the features is presented in Table 9.

A first observation is that the introduction of 3D features improved the aesthetic evaluation. In general, as expected, 3D features contribute to a correct evaluation, both for Physicians #1 and #2. Particularly, the result obtained for Physician #2 is remarkable: a miss detection of 0.14, which is very low in comparison with the error around 30% of the BCCT.core (Cardoso and Cardoso 2007). However, this result may be biased by the evaluation of this specialist, corroborating the need for a panel of experts to reach consensus. The cascade scheme, using the aesthetic evaluation from Physician #1 as reference, and using three classes only, did not improve the initial 2D result. From the results, it is possible to observe that 3DNRA and SAA features appear in almost all selected models, meaning that they have a greater influence on the aesthetic evaluation. However, the results need to be read with caution. More data, both in number

Table 6. Results obtained considering 2D features only.

GT	# Classes	Kernel	C	γ	MER	Corr	Kappa	wKappa	Feat. set
Phy. #1	4	RBF	64	0.5	0.44	0.58	0.33	0.43	[10,12,13,14,16]
	3	RBF	64	0.5	0.36	0.51	0.45	0.47	[10,12,13,14,16]
Phy. #2	3	RBF	64	0.25	0.20	0.66	0.54	0.58	[8,10,12,16,24]

Table 7. Results obtained for the cascade scheme.

GT	# classes	Kernel	C	γ	MER	Corr	Kappa	wKappa	Feat. set
Phy. #1	4	RBF	64	0.5	0.40	0.63	0.40	0.50	[34]
	3	RBF	64	0.5	0.36	0.51	0.45	0.47	[34]
Phy. #2	3	RBF	64	0.25	0.17	0.71	0.59	0.63	[33]

Table 8. Results obtained for the non-restricted scheme of 2D and 3D features.

GT	# classes	Kernel	C	γ	MER	Corr	Kappa	wKappa	Feat. set
Phy.#1	4	RBF	64	0.5	0.43	0.63	0.41	0.51	[9,10,13,14,16,34]
	3	RBF	64	0.5	0.36	0.48	0.45	0.46	[9,10,13,14,16,34]
Phy.#2	3	linear	64	–	0.14	0.81	0.68	0.73	[9,24,32,33,34]

Table 9. Selected features.

#	Acronym	Description
8	pBRA	Dimensionless breast retraction assessment
9	pLBC	Dimensionless lower breast contour
10	pUNR	Dimensionless upward nipple retraction
12	pBCD	Dimensionless breast contour difference
13	pBAD	Dimensionless breast area difference
14	pBOD	Dimensionless breast overlap difference
16	$c\chi^2_a$	χ^2 distance between the histograms in the a channel of the CIE $L*a*b*$
24	$s\chi^2_a$	Surgical scar visibility measured with χ^2 in the a channel of the CIE $L*a*b*$
32	VDA	Volume difference assessment
33	SAA	Surface area assessment
34	3DNRA	3D nipple retraction assessment

and in diversity, with a more robust reference evaluation by specialists, are required to validate the results.

8. Conclusion

This work demonstrated the use of low-cost equipment, the Kinect device, to build a system for the aesthetic evaluation of BCCT with improved automation, robustness, reproducibility and overall cosmetic accuracy. This work takes advantage of both the depth and RGB information acquired with the Kinect. The two are combined in order to take advantage of the best of each data modality. During this work, real images from patients who underwent breast cancer surgery were used. During the project, we always tried to increase the number of cases to improve the robustness and reliability of the methodology. For the construction of the algorithms, we always paid attention to all the questions related to over training and over fitting. In most of the methods, the algorithms were being parameterised with a subset of the complete data, in order to prevent all these issues.

First, depth information is used to extract the complete breast contour and the breast peak point. With this information, after an appropriate RGB-D joint calibration, the breast contour was superimposed on the RGB image to help detect the nipples. All these prominent points are detected automatically, as well as the volumetric information obtained afterwards on the depth map images. It was demonstrated that depth-map images facilitate the automation of the overall system, maintaining BCCT.kore an affordable and easy-to-use tool. Results also confirm an excellent performance and robustness for a wide variety of patients. Some of the results present high variation; however, this is only substantial for the methods that did not work well. For those that present good results the variation is marginal.

Moreover, it was confirmed that the detected volumetric features on Kinect data (nipple height, volume, surface area and 3D nipple retraction) have enough quality for aesthetic quantification. For the particular case of the breast height, the comparison with measurements carried out by physicians provided evidence of the process reliability. The results prove that it is possible to extract reliable 3D information from the Kinect, improving the aesthetic evaluation comparatively with the subjective evaluation carried out by specialists. It is possible to state that 3D features help the overall classification of the aesthetic result; however, more tests, with a broader database, must be conducted to further validate the system. Future work will focus on extracting more reliable volumetric information. The intention is to make a better use of the video frames acquired with the Kinect in order to create a more complete 3D model by registering multiple depth images.

Funding

The first author would like to thank Fundação para a Ciência e Tecnologia (FCT) – Portugal for the financial support for the Ph. D. [grant number SFRH/BD/43772/2008]. This work was financed by the ERDF – European Regional Development Fund through the COMPETE Programme (operational programme for competitiveness) and by National Funds through the FCT within project PTDC/SAU-ENB/114951/2009. The work leading to these results has received funding from the European Community's Seventh Framework Programme [grant number FP7600948].

References

Asgeirsson KS, Rasheed T, McCulley SJ, Macmillan RD. 2005. Oncological and cosmetic outcomes of oncoplastic breast conserving surgery. Eur J Surg Oncol. 31(8):817–823.

Beadle GF, Come S, Henderson IC, Silver B, Hellman S, Harris JR. 1984. The effect of adjuvant chemotherapy on the cosmetic results after primary radiation treatment for early stage breast cancer. Int J Radiat Oncol Biol Phys. 10 (11):2131–2137.

Cardoso JS, Cardoso MJ. 2007. Towards an intelligent medical system for the aesthetic evaluation of breast cancer conservative treatment. Artif Intell Med. 40(2):115–126.

Cardoso JS, daCosta JFP. 2007. Learning to classify ordinal data: the data replication method. J Mach Learn Res. 8:1393–1429.

Cardoso JS, daCosta JFP, Cardoso MJ. 2005a. SVMs Applied to objective aesthetic evaluation of conservative breast cancer treatment. In: Proceedings of the international joint conference on neural networks. Montreal (Canada): IEEE. p. 2481–2486.

Cardoso JS, daCosta JFP, Cardoso MJ. 2005b. Modelling ordinal relations with SVMs: an application to objective aesthetic evaluation of breast cancer conservative treatment. Neural Networks. 18(5–6):808–817.

Cardoso JS, Teixeira LF, Cardoso MJ. 2008. Automatic breast contour detection in digital photographs. In: Proceedings of the international conference on health informatics. Funchal (Portugal): INSTICC. p. 91–98.

Cardoso MJ, Cardoso JS, Santos AC, Barros H, Oliveira MC. 2006. Interobserver agreement and consensus over the esthetic evaluation of conservative treatment for breast cancer. Breast. 15(1):52–57.

Cardoso MJ, Cardoso JS, Vrieling C, Macmillan D, Rainsbury D, Heil J, Hau E, Keshtgar M. 2012. Recommendations for the aesthetic evaluation of breast cancer conservative treatment. Breast Cancer Res Treat. 137:629–637.

Catanuto G, Patete P, Spano A, Pennati A, Baroni G, Nava MB. 2009. New technologies for the assessment of breast surgical outcomes. Aesthetic Surg J. 29(6):505–508.

Chang CC, Lin CJ. 2011. LIBSVM: a library for support vector machines. ACM Trans Intell Syst Technol. 2(3):27:1–27:27.

Christie DRH, O'Brien MY, Christie JA, Kron T, Ferguson SA, Hamilton CS, Denham JW. 1996. A comparison of methods of cosmetic assessment in breast conservation treatment. Breast. 5:358–367.

Duda RO, Hart PE, Stork DG. 2000. Pattern classification. 2nd ed. New York: Wiley Interscience.

Eder M, Waldenfels F, Swobodnik A, Kloppel M, Pape A, Schuster T, Raith S, Kitzler E, Papadopulos N, Machens H, et al. 2012. Objective breast symmetry evaluation using 3-D surface imaging. Breast. 21(2):152–158.

Fisher B, Anderson S, Bryant J, Margolese RG, Deutsch M, Fisher ER, Jeong JH, Wolmark N. 2002. Twenty-year follow-up of a randomized trial comparing total mastectomy, lumpectomy, and lumpectomy plus irradiation for the treatment of invasive breast cancer. New Engl J Med. 347 (16):1233–1241.

Fisher NI, Lee AJ. 1983. A correlation coefficient for circular data. Biometrika. 70(2):327–332.

Gama J, Brazdil P. 2000. Cascade generalization. Mach Learn. 41(3):315–343.

Harris JR, Levene MB, Svensson G, Hellman S. 1979. Analysis of cosmetic results following primary radiation therapy for stages I and II carcinoma of the breast. Int. J Radiat Oncol Biol Phys. 5(2):257–261.

Herrera DC, Kannala J, Heikkila J. 2012. Joint depth and color camera calibration with distortion correction. IEEE Trans Pattern Anal Mach Intell. 34(10):2058–2064.

Jemal A, Bray F, Center MM, Ferlay J, Ward E, Forman D. 2011. Global cancer statistics. CA: Cancer J Clin. 61(2):69–90.

Kim NF, Park JS. 2004. Segmentation of object regions using depth information. In: Proceedings of the international conference on image processing. Singapore: IEEE. p. 231–234.

Kobatake H, Hashimoto S. 1999. Convergence index filter for vector fields. IEEE Trans Image Process. 8(8):1029–1038.

Lee J, Chen S, Reece GP, Crosby MA, Beahm EK, Markey MK. 2012. A novel quantitative measure of breast curvature based on catenary. IEEE Trans Biomed Eng. 59(4):1115–1124.

Limbergen EV, Schueren EV, Tongelen KV. 1989. Cosmetic evaluation of breast conserving treatment for mammary cancer. 1. Proposal of a quantitative scoring system. Radiother Oncol. 16(3):159–167.

Monteiro JC, Oliveira HP, Sequeira AF, Cardoso JS. 2013. Robust Iris segmentation under unconstrained settings. In: Proceedings of the international conference on computer vision theory and applications. p. 180–190.

Moyer HR, Carlson GW, Styblo TM, Losken A. 2008. Three-dimensional digital evaluation of breast symmetry after breast conservation therapy. J Am Coll Surg. 207 (2):227–232.

Oliveira HP, Cardoso JS. 2009. Image retargeting using stable paths. In: Proceedings of the fourth international conference on computer vision theory and applications. Lisbon (Portugal): INSTICC. p. 40–47.

Oliveira HP, Cardoso JS, Magalhaes A, Cardoso MJ. 2012. Simultaneous detection of prominent points on breast cancer conservative treatment images. In: Proceedings of the IEEE international conference on image processing. Orlando (FL): IEEE. p. 2841–2844.

Oliveira HP, Cardoso JS, Magalhaes A, Cardoso MJ. 2013. Methods for the aesthetic evaluation of breast cancer conservation treatment: a technological review. Curr Med Imag Rev. 9(1):32–46.

Oliveira HP, Magalhaes A, Cardoso MJ, Cardoso JS. 2010. An accurate and interpretable model for BCCT.core. In: Proceedings of the 32nd annual international conference of the IEEE engineering in medicine and biology society. Buenos Aires (Argentina): IEEE. p. 6158–6161.

Oliveira HP, Patete P, Baroni G, Cardoso JS. 2011. Development of a BCCT quantitative 3D evaluation system through low-cost solutions. In: Proceedings of the 2nd international conference on 3D body scanning technologies. Corfu (Greece): IEEE. p. 16–27.

Pezner RD, Patterson MP, Hill LR, Vora N, Desai KR, Archambeau JO, Lipsett JA. 1985. Breast retraction assessment: an objective evaluation of cosmetic results of patients treated conservatively for breast cancer. Int J Radiat Oncol Biol Phys. 11(3):575–578.

Sousa R, Cardoso JS, daCosta JFP, Cardoso MJ. 2008. Breast contour detection with shape priors. In: Proceedings of the 15th IEEE international conference on image processing. San Diego (CA): IEEE. p. 1440–1443.

Veronesi U, Cascinelli N, Mariani L, Greco M, Saccozzi R, Luini A, Aguilar M, Marubini E. 2002. Twenty-year follow-up of a randomized study comparing breast-conserving surgery with radical mastectomy for early breast cancer. New Engl J Med. 347(16):1227–1232.